Article | Open Access

Energy Materials

Li *et al*. *Energy Mater.* **2026**, *6*, 600069 **DOI:**10.20517/energymater.2026.67

In-situ construction of artificial interface layer using sodiophilic Bi_2S_3 nanowires for dendritic-free sodium-metal batteries

Jiazhe Li[1,2], Jiyi Li[3], Yu Qiao[1,2], Daxian Cao[3], Xin Ji[2], Weijiang Xue[3,4], Guiyin Xu[1,5], Hengda Sun[1,5], Xiaogang Han[2], Hongkang Wang[1,2,*]

Keywords: Sodium metal anode, sodiophilic Bi_2S_3 nanowires, artificial interface layer, Na^+ diffusion kinetics, dendrite-free plating

Citation: Li, J.; Li, J.; Qiao, Y.; Cao, D.; Ji, X.; Xue, W.; Xu, G.; Sun, H.; Han, X.; Wang, H. *In-situ* construction of artificial interface layer using sodiophilic Bi_2S_3 nanowires for dendritic-free sodium-metal batteries. *Energy Mater.* **2026**, *6*, 600069. https://dx.doi.org/10.20517/energymater.2026.67

Received: 13 Apr 2026
First Decision: 11 May 2026
Revised: 28 May 2026
Accepted: 12 Jun 2026
Published: 29 Jun 2026

Academic Editor: Jiazhao Wang
Copy Editor: Ping Zhang
Production Editor: Ping Zhang

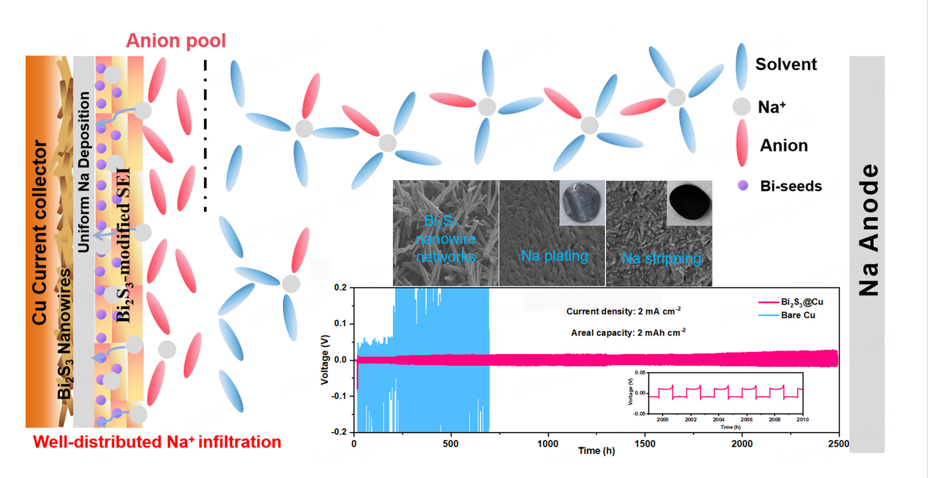

Abstract

Sodium metal anodes possess low redox potential and high theoretical capacity, yet they face the challenges of uncontrolled dendritic growth and unstable solid-electrolyte interphase (SEI). Herein, we report a straightforward synthesis of Bi_2S_3 nanowires, which are engineered as a sodiophilic artificial interface layer to facilitate uniform and dendrite-free Na plating-stripping. Density functional theory (DFT) calculations and experimental characterizations confirm that Bi_2S_3 with high Na^+ adsorption energy undergoes a sequential *in-situ* conversion-alloying reaction with Na^+, forming sodiophilic Na_3Bi alloy nucleation sites and a highly Na^+-conductive Na_2S matrix. This composite interface synergistically lowers the Na nucleation energy barrier and accelerates Na^+ diffusion kinetics, effectively suppressing dendritic Na growth. Besides, Bi_2S_3 displays a stronger affinity of PF_6 anions, facilitating the formation of NaF-rich SEI film with highly stable

---

[1]Pingdingshan Industrial Technology Research Institute, Henan Academy of Sciences, Zhengzhou 450046, Henan, China.
[2]State Key Lab of Electrical Insulation and Power Equipment, Center of Nanomaterials for Renewable Energy (CNRE), School of Electrical Engineering, Xi'an Jiaotong University, Xi'an 710049, Shannxi, China.
[3]State Key Laboratory of Advanced Papermaking and Paper-Based Materials, Plant Fiber Research Center, School of Light Industry and Engineering, South China University of Technology, Guangzhou 510641, Guangdong, China.
[4]Center for Advancing Materials Performance from the Nanoscale (CAMP-Nano), State Key Laboratory for Mechanical Behavior of Materials, Xi'an Jiaotong University, Xi'an 710049, Shannxi, China.
[5]State Key Laboratory for Modification of Chemical Fibers and Polymer Materials, College of Materials Science and Engineering, Donghua University, Shanghai 201620, China.

[*]**Correspondence to:** Dr. Hongkang Wang, State Key Lab of Electrical Insulation and Power Equipment, Center of Nanomaterials for

Renewable Energy (CNRE), School of Electrical Engineering, Xi'an Jiaotong University, Xi'an 710049, Shannxi, China. E-mail: hongkang.wang@mail.xjtu.edu.cn

interface. Benefiting from these advantages, the Na/Bi_2S_3@Cu symmetric cell displays an extraordinary cycling lifespan of over 2,500 h at 2 mA cm^{-2} and 2 mAh cm^{-2}, accompanied by an ultralow overpotential of 15 mV and a negligible interfacial resistance of 7.8 Ω even after 1,350 cycles. When paired with a commercial $Na_3V_2(PO_4)_3$/C cathode, the Na/Bi_2S_3 anode delivers superior long-term cycling stability and high-rate capability with capacity retention of 70% after 2,500 cycles at 10 C. This work provides an effective strategy for constructing stable sodiophilic interfaces for sodium metal anodes, which offers new fundamental insights for achieving high-performance sodium metal batteries.

INTRODUCTION

The energy crisis and environmental pollution have spurred the global pursuit of renewable energy sources (ex., solar and wind), but their intermittent and fluctuating natures calls for the development of low-cost large-scale energy storage technologies to ensure reliable energy supply[1-3]. Lithium-ion batteries (LIBs) have been widely applied in portable electronics and electric vehicles owing to their exceptional energy/power density and long cycling life[4-6]. Nevertheless, the scarcity of lithium resources severely limit their large-scale application, creating an urgent demand for alternative battery systems based on earth-abundant elements[7]. Alternatively, sodium metal batteries (SMBs) have emerged as a promising candidate, thanks to the ubiquitous availability, low cost, and wide distribution of sodium resources[8-10]. Moreover, sodium metal anodes (SMAs) exhibit analogous physical and chemical properties to lithium metal, including a high specific capacity (1,166 mAh g^{-1} in theory) and a low redox potential [-2.71 V *vs.* Standard Hydrogen Electrode (SHE)], making them ideal for fabricating high-energy-density SMBs[11-13]. Despite these inherent advantages, the practical application of SMBs is limited by intractable challenges associated with SMAs, such as uncontrolled dendritic Na growth and the continuous destruction-construction of the solid-electrolyte interphase (SEI) film during repeated plating/stripping cycles[14-17]. These issues lead to low Coulombic efficiency (CE), rapid capacity fading, severe electrolyte consumption, and even safety hazards such as short circuits, which have become the primary bottlenecks hindering the commercialization of SMBs.

To address the above drawbacks of SMAs, extensive strategies have been explored, including the construction of artificial SEI layers[18], optimization of electrolyte compositions and additives[19], modification of current collectors[20,21], and the development of all-solid-state electrolytes[22-24]. Among these approaches, modifying copper current collectors with sodiophilic materials to *in-situ* form stable artificial SEI films has garnered tremendous attention, as it directly regulates Na nucleation and deposition behavior at the electrode/electrolyte interface, effectively suppressing dendrite growth and stabilizing SEI formation[25-27]. Various sodiophilic metallic materials and their compounds have been explored for current collector modification, as they can form reversible Na-based alloys via alloying-dealloying reactions, which effectively lower the Na nucleation energy barrier and induce uniform Na deposition[25,27,28]. For instance, flexible 3D carbon nanofiber frameworks anchored with Sb nanoparticles or encapsulated with ultrafine Sb_2S_3 nanoparticles have been demonstrated to enable stable Na plating/stripping for over 1,000 h and 2,800 h, respectively, by *in-situ* forming sodiophilic Na_3Sb sites and high Na^+-conductive Na_2S matrices[25,27]. Additionally, CeF_3@N-doped carbon and Na-Sn alloy-based porous carbon composites have been developed to construct NaF-rich SEI layers[10,26], achieving ultra-long cycling stability for SMAs under various test conditions. These studies confirm that the rational design of sodiophilic interfaces with both preferential nucleation sites and high ion-conductive matrices is the key to realizing dendrite-free Na deposition.

Bismuth (Bi) and its derivatives have attracted increasing interest as sodiophilic modifiers due to their strong Na adsorption affinity and reversible Na-Bi alloying behavior[29-31]. However, most reported Bi-based modifiers rely on metallic Bi nanoparticles or Bi/carbon composites, while Bi chalcogenides (e.g., Bi_2S_3) have rarely been explored as precursors for *in-situ* constructing composite sodiophilic interfaces. Bi_2S_3 possesses a unique layered crystal structure and inherent sodiophilicity, and its electrochemical reaction with Na^+ can theoretically generate both Na-Bi alloy nucleation sites and Na_2S ion-conductive matrices- two key components for stabilizing SMAs- via a one-step conversion-alloying process. Furthermore, the nanostructured design of Bi_2S_3 (e.g., nanowires) could provide a porous framework to accommodate the volume change during Na plating/stripping.

Herein, we report the solvothermal synthesis of one-dimensional Bi_2S_3 nanowires and their application as a sodiophilic artificial interface layer on Cu current collectors for high-stability SMAs. The Bi_2S_3 nanowires undergo *in-situ* electrochemical conversion-alloying with Na^+ to form a composite interface consisting of sodiophilic Na_3Bi alloy sites and highly Na^+-diffusive Na_2S matrices, which is further covered by a NaF-rich artificial SEI film. Density functional theory (DFT) calculations reveal that Bi_2S_3 and its electrochemical derivatives exhibit much higher Na^+ adsorption energies than bare Cu, while Na_2S possesses a significantly higher Na^+ diffusion coefficient than conventional SEI components (Na_2O, NaF). Consequently, the construction of Bi_2S_3 nanowire layer efficiently reduced the Na nucleation energy barrier, accelerated Na^+ diffusion kinetics and provided sufficient space to buffer volume expansion during Na plating/stripping. Thus, the Na/Bi_2S_3@Cu symmetric cell achieves a long lifespan of over 2,500 h with an ultralow overpotential of 15 mV at 2 mA cm^{-2} and 2 mAh cm^{-2}. When pairing with commercial $Na_3V_2(PO_4)_3$/C (NVP/C) cathode, the SMB full-cells also exhibit excellent cycling performance and high-rate capability. This work not only develops a simple strategy for constructing stable sodiophilic interfaces for SMAs, but also provides new fundamental insights for the design of chalcogenide-based precursors for *in-situ* forming composite artificial SEI layers, paving the way for the development of high-performance SMBs.

EXPERIMENTAL

Materials synthesis

Bi_2S_3 nanowires were prepared via solvothermal method. In a typical synthesis, 1 mmol bismuth chloride ($BiCl_3$, Macklin) and 1.5 mmol thiourea (CH_4N_2S, Sigma-Aldrich) were completely dissolved in 40 mL ethylene glycol ($C_2H_6O_2$, Alfa Aesar) under magnetic stirring, which were then sealed and reacted in a 100 mL autoclave at 180 °C for 10 h. After cooling down, the precipitate was collected and washed using water and ethanol via centrifugation for several times, finally vacuum drying at 80 °C overnight.

Materials characterizations

X-ray diffraction (XRD) patterns of the products were recorded on a Bruker D2 Phaser diffractometer (Bruker, Germany). The microstructures of the products were characterized by scanning electron microscope (SEM, FEI Company Quanta 250F; FEI, USA) and transmission electron microscope (TEM, JEOL JEM-200; JEOL, Japan). High-Angle Annular Dark-Field Scanning Transmission Electron Microscopy (HAADF-STEM) images and Energy Dispersive X-ray Spectroscopy (EDS) maps were also taken on the JEM-200 TEM instrument (JEOL, Japan). X-ray photoelectron spectroscopy (XPS) was performed on a Thermo Fisher ESCALAB 250Xi instrument (Thermo Fisher Scientific, USA). Time-of-Flight Secondary Ion Mass Spectrometry (TOF-SIMS) was carried out on an ION-TOF instrument (ION-TOF GmbH, Germany).

Electrochemical measurements

All the cells were fabricated/disassembled in an Ar-filled glovebox. The Bi_2S_3 nanowires were deposited onto Cu substrate by casting a slurry, which was consisting of Bi_2S_3 and Polyvinylidene fluoride (PVDF) (HSV900, Arkema) in the ratio of 9:1 in N-methyl-2 pyrrolidinone (NMP, Macklin), and the as-prepared Bi_2S_3@Cu substrate was dried at 60 °C overnight. The loading amount of Bi_2S_3 on Cu foils is approximately 3 mg cm^{-2}. For fabrication of Na metal anodes, certain amount of Na was galvanostatically plated onto the bare Cu and

Bi_2S_3@Cu substrates in asymmetrical cells at various current densities (1.0-10 mA cm^{-2}), thus producing Na pre-deposited Cu or Bi_2S_3@Cu anodes (denoted as Na@Cu or Na/Bi_2S_3@Cu). Symmetrical cells were fabricated by paring two identical electrodes. For both asymmetrical and symmetrical cells, 1.0 M $NaPF_6$ in diglyme was the electrolyte, and Celgard 2400 polypropylene membrane was separator.

For the full cell assembly, the cathode electrodes were fabricated by casting the well-mixed slurry, which is consisting of commercial $Na_3V_2(PO_4)_3$/C (NVP/C), Super P, and PVDF with weight ratio of 8:1:1 in NMP, using Al foil as current collector. The cathode electrodes were cut into a disk shape with Ø of 12 mm and a loading amount of ~2.0 mg cm^{-2}. Whatman glass microfiber membrane was employed as the separator. The Na/Bi_2S_3@Cu with pre-deposition capacity of 3 mAh cm^{-2} was used as the anode, while the electrolyte was identical to that for the symmetric cells. The injection amounts of the electrolyte for symmetric cells and full cells were 40 and 80 μL, respectively. Galvanostatic discharge/charge (GCD) tests were performed using a NEWARE BTS in 2.5-3.8 V. Cyclic voltammetry (CV, 0.01-2.5 V) and electrochemical impedance spectroscopy (EIS, 0.01-10 MHz) were measured on CHI600 electrochemical workstation.

Calculation method

Vienna Ab initio Simulation Package (VASP), which is based on the DFT, was employed to perform first-principles calculations. The electron-ion interactions were described using the Projector Augmented Wave (PAW) method. The valence electronic configurations of the elements considered were Bi ($6s^2$ $6p^3$), S ($3s^2$ $3p^4$), Na ($3s^1$), O ($2s^2$ $2p^4$), and F ($2s^2$ $2p^5$). A plane-wave cutoff energy of 480 eV was used throughout. Brillouin zone integrations were performed using a Monkhorst-Pack k-point grid of 2 × 2 × 2, corresponding to a k-spacing of approximately 0.1 $Å^{-1}$. The electronic self-consistent field (SCF) convergence criterion was set to 10^{-7} eV. Structural optimizations were carried out using the conjugate gradient algorithm until the residual forces on all atoms were below 0.01 eV/Å. The resulting ground-state total energies and relaxed structures were subsequently analyzed. The adsorption energy (E_{ads}) is calculated by $E_{ads} = E_{total} - E_{substrate} - E_{adsorbate}$. Herein, E_{total} is the total energy of the system after the adsorbate is adsorbed on the adsorbent surface, $E_{substrate}$ is the energy of the adsorbent, and $E_{adsorbate}$ is the energy of the isolated adsorbate.

RESULTS AND DISCUSSION

Figure 1A shows the SEM image of the as-synthesized Bi_2S_3 product via solvothermal method, which exhibits well-defined one-dimensional nanowire-like morphology with lengths up to tens of micrometers. Moreover, the nanowires tend to hierarchically bundle at one end. Figure 1B shows the TEM image of a single Bi_2S_3 nanowire with inset showing the Selected Area Electron Diffraction (SAED) pattern, revealing its single-crystalline structure. As shown in the High-Resolution Transmission Electron Microscopy (HRTEM) image [Figure 1C], two sets of lattice fringes with interplanar distances of 0.8 nm and 0.4 nm can be clearly observed, which can be correspondingly indexed to the (101) and (20-2) crystallographic planes of Bi_2S_3[32]. In addition, the angle between (101) and (20-2) is measured as about 90°, which is consistent with the SAED pattern analysis. Figure 1D displays the HAADF-STEM image of a bundle of Bi_2S_3 nanowires which are apparently rooted together at one end. Furthermore, the corresponding EDS analysis shows that the elemental maps for Bi and S are well overlapped within the nanowires [Figure 1E and F], confirming the homogeneous elemental distribution, uniform stoichiometry, and high phase purity of the as-synthesized Bi_2S_3 nanowires.

Figure 1G presents the XRD pattern of the Bi_2S_3 product, where all the diffraction peaks can be well indexed to the orthorhombic phase of Bi_2S_3 (JCPDS No.97-017-1864) with high purity[32]. The inset of Figure 1G schematically illustrates the supercell structure of Bi_2S_3, which consists of tightly bound ribbons extending

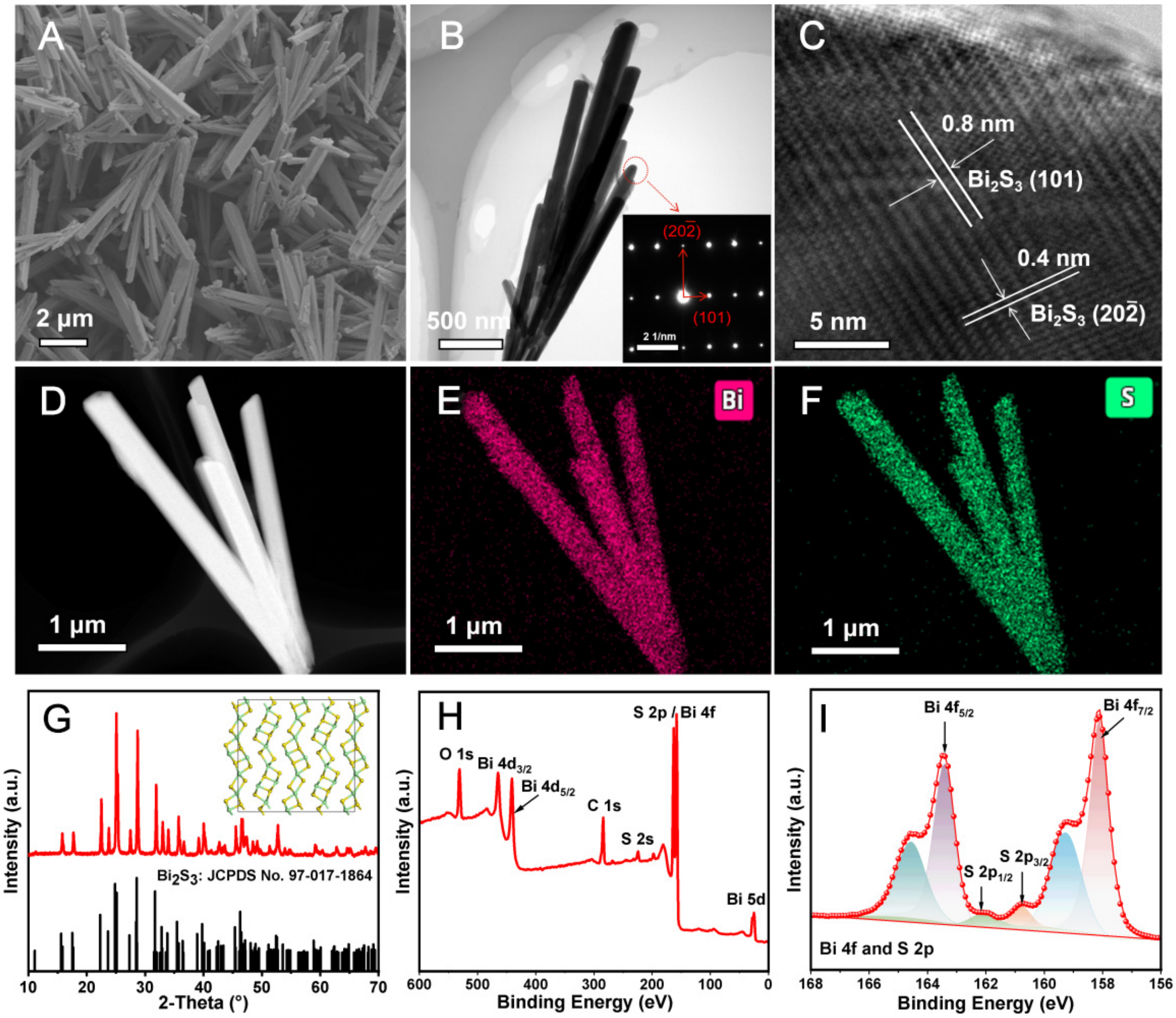

Figure 1. (A) SEM image, (B) TEM image with SAED pattern, and (C) HRTEM image of Bi_2S_3 nanowires; (D) HAADF-STEM image and (E and F) corresponding EDS maps of (E) Bi and (F) S elements for a bundle of Bi_2S_3 nanowires; (G) XRD pattern with inset showing the supercell structure of Bi_2S_3¬ (Yellow balls stand for Bi atomic sites, and green balls for S atoms); (H) Survey XPS spectrum, and (I) Bi 4f/S 2p XPS spectra of Bi_2S_3 nanowires. SEM: Scanning electron microscope; TEM: transmission electron microscope; XPS: X-ray photoelectron spectroscopy; XRD: X-ray diffraction; HRTEM: high-resolution transmission electron microscopy; HAADF-STEM: high-resolution transmission electron microscopy; SAED: selected area electron diffraction.

along the (011) direction[33], and this is consistent with the HRTEM analysis [Figure 1C]. Figure 1H presents the survey XPS spectrum of the Bi_2S_3 product, where characteristic peaks of Bi and S elements are apparently observed. Additionally, O 1s and C 1s signals are present, which are likely attributed to surface adsorption of atmospheric species. Figure 1I displays the XPS spectrum of Bi 4f along with S 2p, in which two pairs of strong doublet peaks locate at 164.6/159.2 eV and 163.5/158.1 eV, corresponding to the Bi $4f_{5/2}$/Bi $4f_{7/2}$ with the chemical state of Bi^{3+} in the Bi-S and Bi-O, respectively. In addition, two minor peaks located at 161.9 eV and 160.7 eV are assigned to S $2p_{1/2}$ and S $2p_{3/2}$, respectively, suggesting the presence of S^{2-} species[34]. Moreover, the high-resolution S 2s XPS spectrum exhibits a peak at 225.6 eV [Supplementary Figure 1], further confirming the sulfide state in the Bi_2S_3 nanowires. The coexistence of bismuth and sulfur spectral features confirms the successful formation of Bi-S bonds within the synthesized product.

Figure 2A shows the CV profile of the Bi_2S_3 electrode in the first cycle, highlighting its characteristic sodiation and desodiation behavior. In the cathodic scan, three distinct reduction peaks locate at approximately 1.00, 0.63 and 0.44 V, which are consistent with the voltage plateaus in the galvanostatic

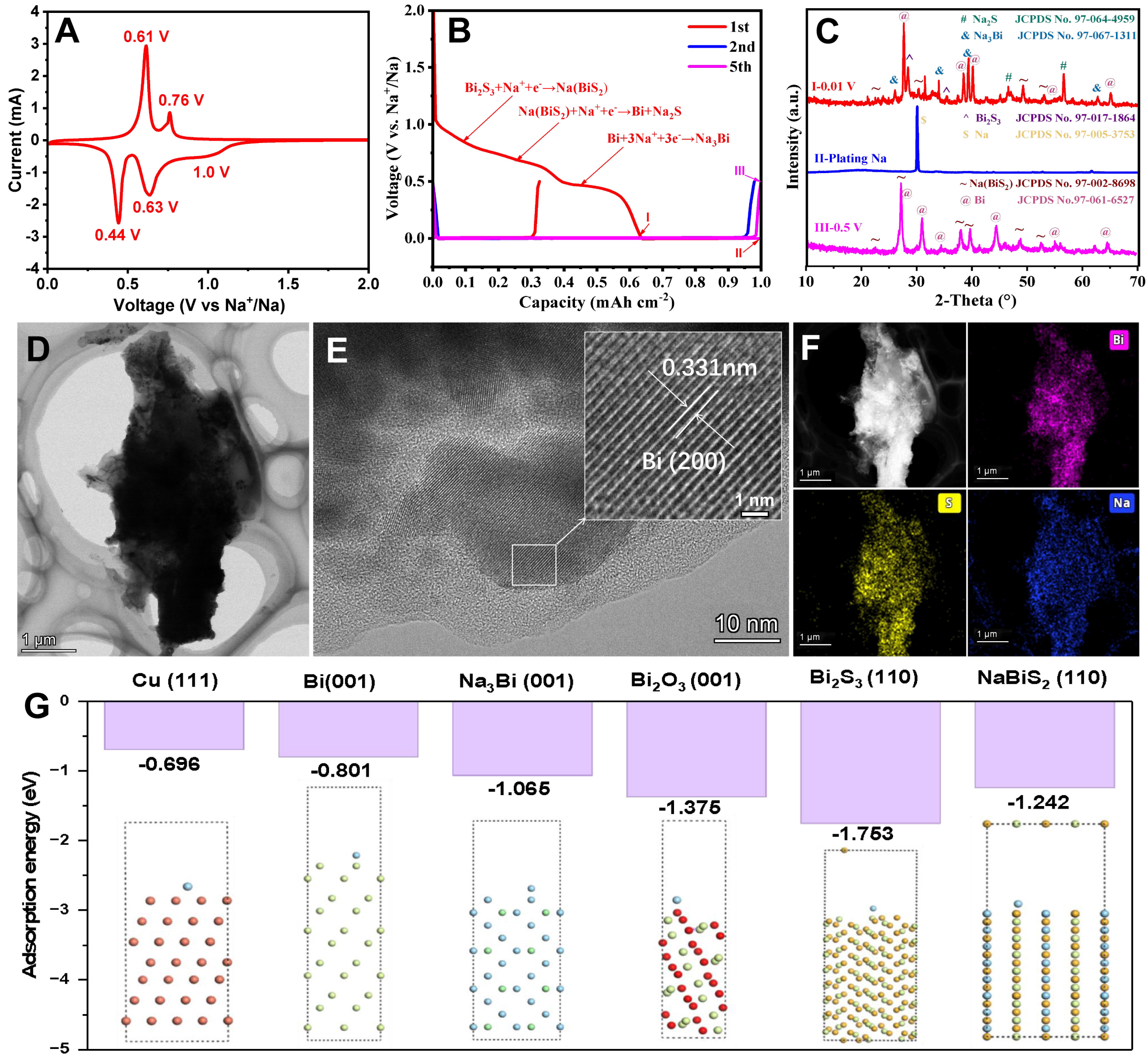

Figure 2. (A) Initial CV curve and (B) GCD curves of Bi_2S_3; (C) XRD patterns of the discharged Bi_2S_3 electrodes at different states; (D) TEM image and (E) HRTEM image of sodiated Bi_2S_3 at initially discharged to 0.5 V, and (F) HAADF-STEM image with corresponding EDS maps of Bi/S/Na elements; (G) Sodium adsorption energies on Cu (111), Bi (001), Na_3Bi (001), Bi_2O_3 (001), Bi_2S_3 (110) and $NaBiS_2$ (110) surfaces, where more negative values imply stronger adsorption. CV: Cyclic voltammetry; GCD: Galvanostatic discharge; XRD: X-ray diffraction; TEM: transmission electron microscope; HRTEM: high-resolution transmission electron microscopy; HAADF-STEM: high-resolution transmission electron microscopy; EDS: energy dispersive X-ray spectroscopy.

discharge profile [Figure 2B]. The minor peak at 1.00 V is related to the Na^+ intercalation into the Bi_2S_3 lattice ($Bi_2S_3 + Na^+ + e^- \rightarrow NaBiS_2$), while the strong peak at 0.63 V corresponds the reduction of $NaBiS_2$ into metallic Bi ($NaBiS_2 + Na^+ + e^- \rightarrow Bi + Na_2S$). Furthermore, the sharp peak at 0.44 V is assigned to the alloying reaction ($Bi + Na^+ + e^- \rightarrow Na_3Bi$)[34]. In the anodic scan, two distinct peaks locate at 0.61 V and 0.76 V, which correspond to the dealloying of Na_3Bi and the oxidation of metallic Bi, respectively.

To further elucidate the structural evolution upon sodiation, *ex-situ* XRD analyses were conducted on the cycled Bi_2S_3 electrodes at different states. When initially discharging to 0.01 V, Bi_2S_3 was electrochemically reduced into Bi and then Na_3Bi alloy, accompanied by the final formation of Na_2S, which was confirmed by the XRD pattern (Figure 2C, pattern I). At this state of 0.01 V, the diffraction peaks for Bi_2S_3 almost disappeared, while new peaks emerge that match with cubic Na_2S (JCPDS No. 97-064-4959), metallic Bi

(JCPDS No. 97-006-4704), Na_3Bi alloy (JCPDS No. 97-067-1311) and cubic $NaBiS_2$ (JCPDS No. 97-002-8698). Further after plating a capacity of 1 mAh cm^{-2}, only XRD pattern for Na metal appears, suggesting the Na deposition on top of the Bi_2S_3-derived substrate. When initially stripped and charged to 0.5 V, the initial Coulombic efficiency is as low as 32%, suggesting large amount of Na was implanted into Bi_2S_3 serving as preferential nucleation sites. In addition, XRD pattern reveals the formation of Bi and $NaBiS_2$ after stripping to 0.5 V in the 5th cycle, and both display high Na^+ adsorption energies, which facilitate the uniform Na plating in the following cycles. Figure 2D depicts the TEM image of the discharged $Bi_2S_{¬3}$ nanowire at 0.5 V, which shows the well retained 1D morphology after sodiation. Figure 2E shows the HRTEM image of the discharged electrode, where metallic Bi nanograins are embedded within the Na_2S matrices, and the enlarged lattice fringes with d-spacing of 0.331 nm can be ascribed to the (200) plane of metallic Bi. Figure 2F displays the HAADF-STEM image of the discharged $Bi_2S_{¬3}$ nanowire with corresponding EDS mapping of Bi, S and Na elements, which are uniformly distributed within the nanowire.

Figure 2G reveals the sodium adsorption energies on Cu (111), Bi (001), Na_3Bi (001), Bi_2O_3 (001), Bi_2S_3 (110) and $NaBiS_2$ (110) surfaces. The calculated adsorption energies are negative, indicating that these adsorptions are exothermic processes. The equivalent values are -1.753, -1.242, -1.375, -1.065 and -0.801 eV for Bi_2S_3 (110), $NaBiS_2$ (110), Bi_2O_3 (001), Na_3Bi (001) and Bi (001), respectively, which are more negative than of Cu (111) (-0.696 eV), suggesting the stronger adsorption and higher interfacial binding energies on the Bi-based substrates. Thus, the Bi_2S_3 surfaces are highly sodiophilic with greater affinity ability to anchor Na^+ ions, as compared to metallic Bi and its alloy or oxide counterparts, which are critical for the uniform Na nucleation and subsequent plating. Additionally, Bi_2S_3 upon sodiation would produce $NaBiS_2$, metallic Bi and finally Na-Bi alloy sequentially, which also show more sodiophilic ability than that for bare Cu substrate, leading to the reduction of the energy barrier for Na nucleation. In order to study the Na^+ diffusion behavior with different sodium-based compounds, the diffusion coefficients of Na_2O, Na_2S, and NaF were calculated via DFT calculation (see details in supporting information) and compared in Supplementary Figure 2 and Supplementary Table 1. The findings indicate that the diffusion coefficient of Na_2S (7.120×10^{-9} cm^{-2}/s) is much higher than those of Na_2O (5.551×10^{-10} cm^{-2}/s) and NaF (1.548×10^{-10} cm^{-2}/s), suggesting the type of anions has a pronounced affection on the diffusion behaviors of sodium-based compounds, as the anionic structural properties greatly affect the lattice density and ion mobility. Importantly, due to the much higher diffusion coefficient of Na_2S[25], it could effectively alleviate the volume expansion of Na-Bi alloying and facilitate the homogeneous distribution of sodium ion flux[35].

To evaluate the reversibility of sodium plating/stripping during cycling, asymmetric cells were fabricated using Bi_2S_3@Cu (or Cu) foils as sodium plating substrates and bare Na foil as counter electrode. As illustrated in Figure 3A, the sodium plating on Bi_2S_3@Cu exhibits a lower nucleation overpotential of only 7 mV than that for the Cu electrode (43 mV) at 1 mA cm^{-2}. The small overpotential can be attributed to the highly sodiophilic nature of Bi_2S_3 and its derivates (ex., Bi and Na-Bi alloy) with higher adsorption energies, which facilitate the uniform sodium nucleation and enhance homogeneous sodium deposition, and this is supported by the DFT calculations [Figure 2G]. Figure 3B compares the Coulombic efficiencies (CEs) of the Na plating/stripping on Bi_2S_3@Cu and Cu substrates upon cycling at 5 mA cm^{-2} with 1 mAh cm^{-2}, and CE as a critical indicator reveals the electrochemical stability, which is defined as a capacity ratio of sodium stripping to plating in each cycle. Apparently, the sodium plating/stripping on the Bi_2S_3@Cu electrode demonstrates highly stable CEs with values of up to 99.9% during 1,000 cycles, indicating the extremely high reversibility of the sodium plating/stripping process. In contrast, the bare Cu electrode exhibits significant CE variations and loses functionality after tens of cycles, which have been attributed to unstable SEI formation and mossy Na deposition[36].

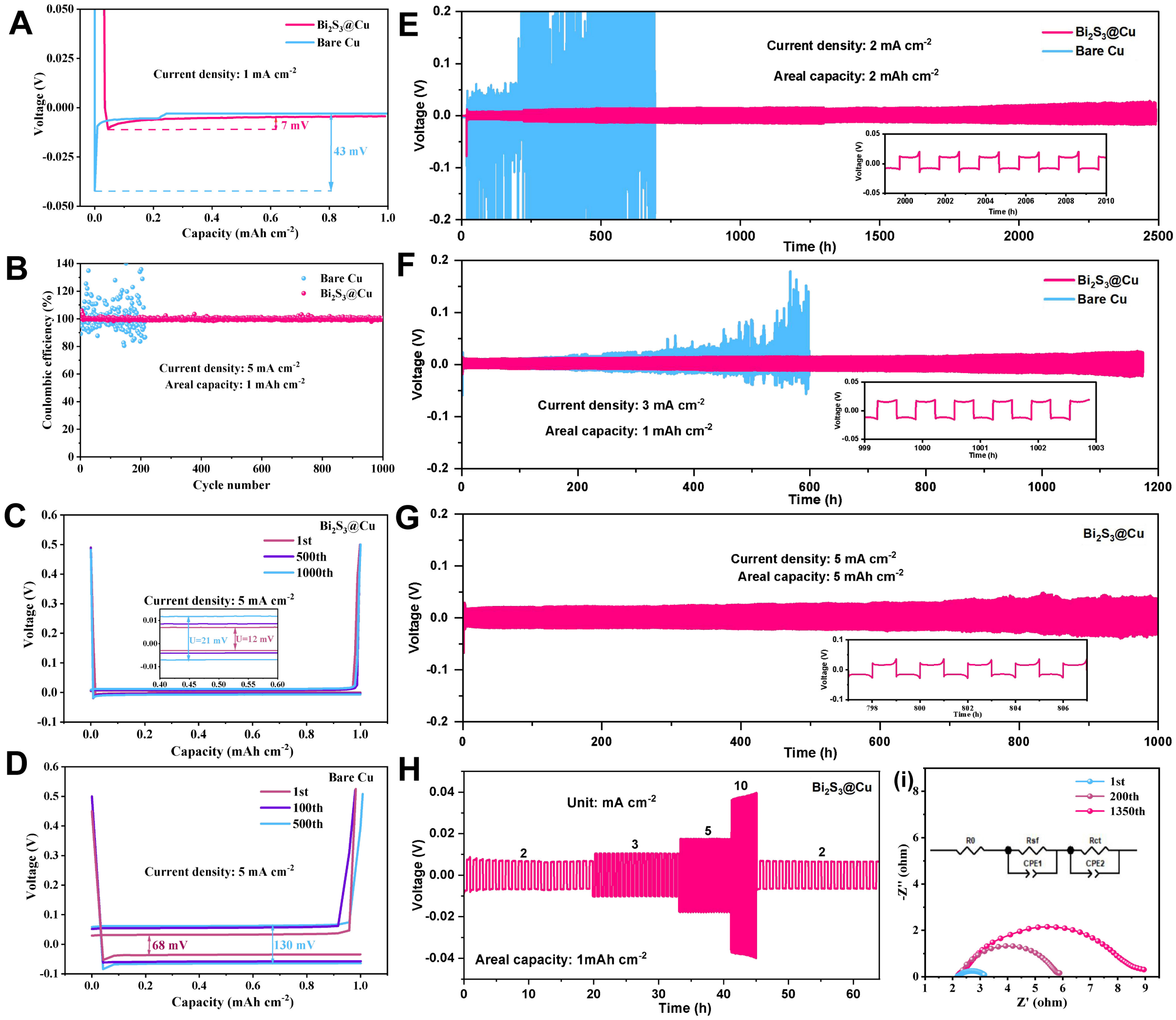

Figure 3. (A) Galvanostatic Na plating profiles on the bare Cu and Bi_2S_3@Cu substrates at 1 mA cm^{-2}; (B) Comparison of CEs upon Na plating/stripping cycling on the Cu and Bi_2S_3@Cu substrates at 5 mA cm^{-2} and 1 mAh cm^{-2}; (C and D) Voltage-capacity curves of sodium plating/stripping processes on Bi_2S_3@Cu substrate (C) and Cu substrate (D) at 5 mA cm^{-2}; (E-G) Voltage-time profiles of symmetric cells of Na/Bi_2S_3@Cu and Na@Cu electrodes at (E) 2 mA cm^{-2} and 2 mAh cm^{-2}, (F) 3 mA cm^{-2} and 1 mAh cm^{-2}, and (G) 5 mA cm^{-2} and 5 mAh cm^{-2}, with insets displaying magnified views of selected cycles; (H) Rate performance of Na/Bi_2S_3@Cu symmetric cells tested at current densities ranging from 2 mA cm^{-2} to 10 mA cm^{-2} with a fixed capacity of 1 mAh cm^{-2}; (I) Nyquist plots of Na/Bi_2S_3@Cu symmetric cells after different cycles. CEs: Coulombic efficiencies.

Figure 3C displays the voltage-capacity profiles of the sodium plating/stripping on the Bi_2S_3@Cu electrode, which are highly overlapped with voltage hysteresis increasing only slightly from 21 mV in the first cycle to 42 mV after 1,000 cycles at 5 mA cm^{-2} and 1 mAh cm^{-2}. In comparison, the Na plating/stripping on bare Cu substrates displays larger voltage hysteresis, escalating from 68 mV (1st cycle) to 130 mV (500th cycle) under the same condition [Figure 3D], along with inferior cycling stability. These results confirm that the construction of sodiophilic Bi_2S_3 buffering layer on Cu substrate significantly enhances the reversibility of sodium plating/stripping, which efficiently suppress the interfacial side reactions and uncontrolled dendrite growth.

To evaluate the efficacy of Bi_2S_3 in suppressing sodium dendrite growth, symmetric cells were assembled using two identical electrodes. As depicted in Figure 3E, the Na/Bi_2S_3@Cu-based symmetric cell demonstrates exceptional long-term sodium plating/stripping stability with a lifespan of 2,500 h and a low overpotential of

15 mV at 2 mA cm^{-2} and 2 mAh cm^{-2}. In contrast, the bare Na@Cu-based symmetric cell exhibits unstable sodium plating/stripping behavior, with the overpotential abruptly exceeding 0.5 V after 260 h, indicating severe polarization under identical current conditions. Even at 3 mA cm^{-2} and 1 mAh cm^{-2} [Figure 3F], the Na/Bi_2S_3@Cu-based symmetric cell still achieved a long stable lifespan of over 1,200 h with a small overpotential of 21 mV. Comparatively, the bare Na@Cu-based symmetrical cell displays apparent voltage variations with gradually increased overpotentials, and a steep increase after around 600 h. It's noteworthy that the voltage-time profiles of Na/Bi_2S_3@Cu-based symmetric cells at various cycles exhibit well-approximated square waves [Figure 3F], indicating the suppression of sodium dendrite growth and interfacial side reactions[37]. By comparison, the bare Na@Cu-based cell shows highly irregular voltage-time curves, suggesting the formation of disordered sodium dendrites and the continuous SEI breaking/repairing, which would lead to unnecessary electrolyte consumption and finally result in battery failure.

Figure 3G depicts the voltage-time profiles of the Na/Bi_2S_3@Cu-based symmetric cells at 5 mA cm^{-2} and 5 mAh cm^{-2}, which still exhibits highly reversible sodium plating/stripping behavior for over 1,000 h, exhibiting a low overpotential of 33 mV. Moreover, Figure 3H shows the rate performance rate of the Na/Bi_2S_3@Cu-based symmetrical cell, which was test at a capacity of 1 mAh cm^{-2} with varied current densities ranging from 2 to 10 mA cm^{-2}. Remarkably, the cell displayed small overpotentials of 6.7, 10.4, 17.5 and 39.4 mV at current densities of 2, 3, 5 and 10 mA cm^{-2}, respectively. When recovering the current density to 2 mA cm^{-2}, an overpotential of 6.6 mV can be achieved. These results highlight the excellent rate performance of the Na/Bi_2S_3@Cu electrode and the robustness of Bi_2S_3 buffering layer on suppressing the sodium dendrite growth and regulating the uniform sodium deposition. To better understand the excellent sodium plating/stripping behavior, EIS was carried out on the symmetric cells. Figure 3I displays the Nyquist plots of Na/Bi_2S_3@Cu symmetric cells after different cycles, which show low interfacial resistances of 1.1, 5.8 and 7.8 Ω after 1st, 200th and even 1350th cycles, corroborating the significantly enhanced electrochemical stability. The excellent sodium plating/stripping performance of Na/Bi_2S_3@Cu electrode could be primarily attributed to the construction of sodiophilic Bi_2S_3 buffering layer with higher sodium adsorption energy, which in situ converted into sodiophilic Bi and Na-Bi grains, as well as the Na_2S matrices with higher sodium diffusion coefficients. These characteristics are highly beneficial for uniform sodium plating. Moreover, Supplementary Figure 3 and Supplementary Table 2 summarized the electrochemical performances of various sodium metal anodes, and the Na/Bi_2S_3@Cu symmetric cell also displayed outstanding overall performance.

Figure 4A schematically illustrates the different Na plating behaviors on the bare Cu and Bi_2S_3@Cu substrates. It's well recognized that the coarse surface of bare Cu substrate usually leads to the random sodium nucleation and non-uniform deposition with un-avoided dendrite formation[38,39]. In contrast, owing to the high adsorption energy of Bi_2S_3, the sodium ions are anchored and readily reacted with Bi_2S_3 in the initial plating stage, forming sodiophilic Bi and Na-Bi grains which were embedded into the Na_2S matrices with high sodium ion diffusivity. These sodiophilic grains thus facilitate the homogeneous sodium nucleation and subsequent uniform dendrite-free sodium deposition, which were verified by the *ex-situ* SEM analysis. Figure 4B shows the SEM image of Na-plated Cu substrate with areal capacity of 1 mAh cm^{-2} at 1 mA cm^{-2} after 70 cycles, apparently displaying mossy and dendritic Na morphologies, while the silver-like Na metal on Cu substrate displays apparently rough surface and uneven distribution (inset of Figure 4B). After subsequent stripping, dead Na can be observed, further confirming the dendrite formation [Figure 4C].

Supplementary Figure 4 reveals that the pristine Bi_2S_3 nanowires are coated onto the Cu substrate, forming porous nanowire networks, within which the volume can efficiently accommodate the expansion after Na deposition. Consequently, with Bi_2S_3 nanowire networks as an artificial buffering layer, the Bi_2S_3@Cu effectively achieve the uniform Na plating/stripping [Figure 4D-G]. Figure 4D shows the SEM image of

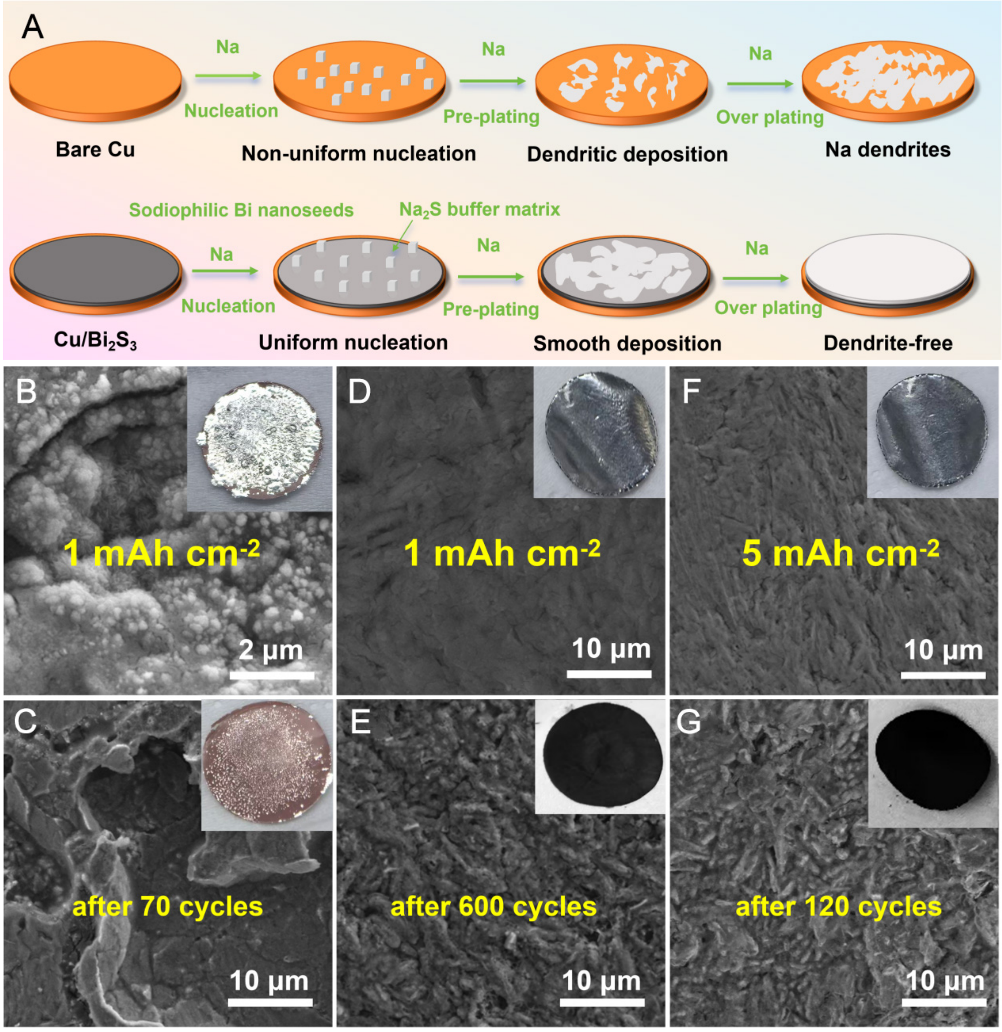

Figure 4. (A) Scheme illustrating the distinct Na plating behaviors on bare Cu and Bi$_2$S$_3$@Cu substrates; (B and C) *Ex-situ* SEM images of the bare Cu substrate after Na plating (B) and stripping (C) at 1 mA cm^{-2} with 1 mAh cm^{-2} after 70 cycles; (D-G) *Ex-situ* SEM images of the Bi$_2$S$_3$@Cu substrate after Na plating (D and F) and stripping (E and G) at 1 mA cm^{-2} with 1 mAh cm^{-2} (D and E) after 600 cycles and at 1 mA cm^{-2} with 5 mAh cm^{-2} (F and G) after 120 cycles. Insets of (B-G) show the optical photographs of the electrodes after Na plating and stripping. SEM: Scanning electron microscope.

Na-plated Bi$_2$S$_3$@Cu after 600 cycles at 1 mA cm^{-2} and 1 mAh cm^{-2}, where no Na-dendrite can be observed, and photo of the electrode displays uniform silver-like Na metal layer with smooth surface. Even at a higher areal capacity of 5 mAh cm^{-2} after 120 cycles [Figure 4F], both SEM image and electrode photo reveal the uniform Na depositon without dendrite formation. Oppositely, after complete Na-stripping, the photos of the desodiated Bi$_2$S$_3$@Cu electrodes display dark in color, and no silver-like "dead Na" appears. Interestingly, the cycled Bi$_2$S$_3$ nanowires still retain the 1D morphology [Figure 4E and G], but their volumes are expanded owing to the volume changes after repeated sodiation/desodiation cycling. Remarkably, no mossy or dead Na are observed in the Bi$_2$S$_3$@Cu electrode even upon long-term plating/stripping cycling, suggesting Bi$_2$S$_3$ effectively inhibits the sodium dendrite formation.

Moreover, *in-situ* optical microscopy was further applied to dynamically observe the sodium plating/stripping process on the bare Cu and Bi$_2$S$_3$@Cu substrates in asymmetric batteries. As shown in Supplementary Figure 5A-D, upon plating at 1 mA cm^{-2} for 60 min, the cross-section of Bi$_2$S$_3$@Cu maintains flat topography throughout the cycling process, indicating no apparent dendrite generation and the superior dendrite inhibition effect of Bi$_2$S$_3$ layer. But for bare Cu substrate, localized bright spots can be apparently

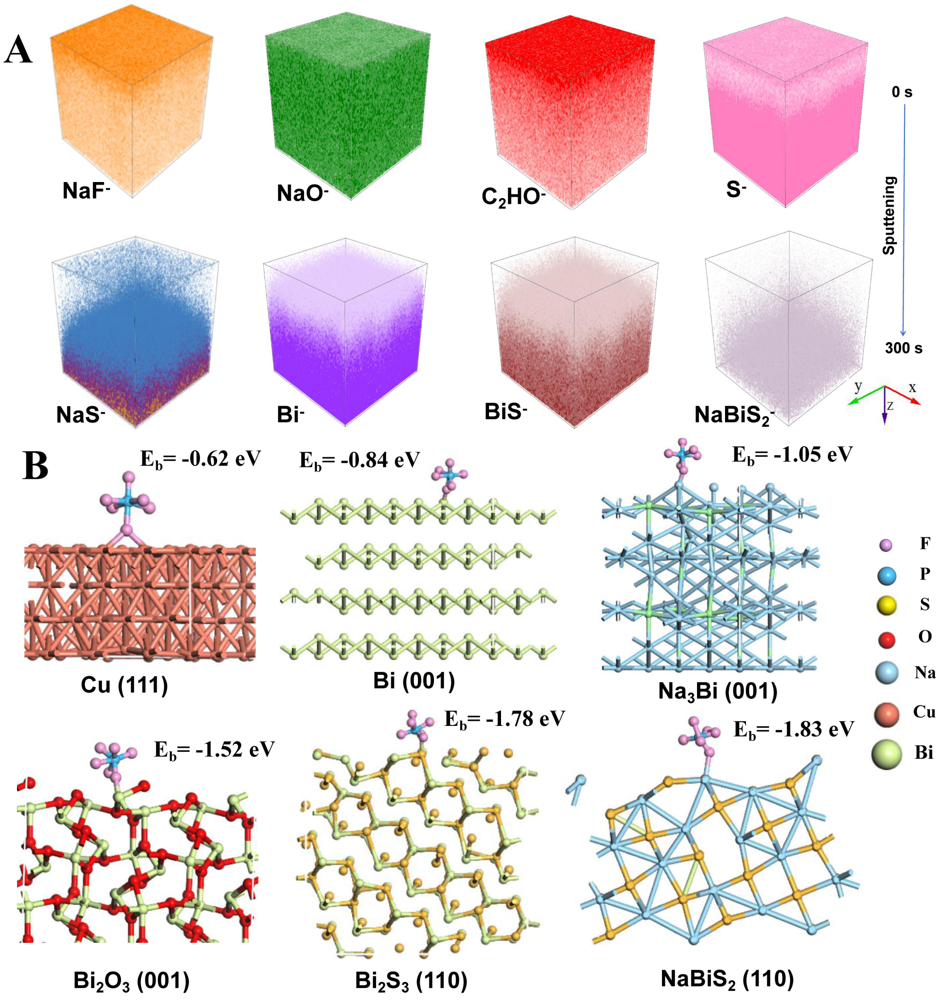

Figure 5. (A) 3D-mapping images of different secondary ion fragments of the Na-stripped Bi_2S_3@Cu after 10 cycles at 0.5 mA cm^{-2} and 3 mAh cm^{-2}; (B) Binding energy and adsorption site of PF_6 on Cu (111), Bi (001), Na_3Bi (001), Bi_2O_3 (001), Bi_2S_3 (110) and $NaBiS_2$ (110).

observed after about 15 min of plating [Supplementary Figure 5E-H], suggesting the formation of sodium bulks and dendrites, and this can be explained by the tip discharge effect due to the inhomogeneous electric field on the surface[40]. Such sharp contrast further highlight the critical role of Bi_2S_3 in enabling the homogenous deposition of sodium and good inhibition of dendrite growth[41].

To investigate the composition and chemical situations of the Bi_2S_3 induced artificial interface layer, *ex-situ* TOF-SIMS analysis was performed on the Na-stripped Bi_2S_3@Cu after 10 cycles [Figure 5A], revealing the presence of broken inorganic fragments (ex., NaF^-, NaO^-, NaS^-, $NaBiS_2^-$, *etc.*) and organic derivatives (C_2HO^-, arising from the decomposition of solvent molecules). As revealed by the 3D-mapping images with in-depth profiling along z-axis, NaF^- and NaO^- species are well distributed within the SEI layer, while C_2HO^- mainly presents in the surface region. In contrast, Bi/S-related species (ex., NaS^-, $NaBiS_2^-$) predominantly exist in the inner region, indicating the SEI layer is rich in inorganic species, which are covered on the sodiophilic Bi_2S_3-related derivates. Consequently, the Bi_2S_3-induced artificial SEI layer with uniform distribution of different inorganic phases facilitates the well-distributed Na^+ infiltration at the same rate, thus leading to the uniform Na deposition[26,42,43].

To investigate the interactions of PF_6 anion with different substrates, DFT simulations were performed to calculate the binding energies (E_b) of PF_6 anion on various substrates. It's worth noting that the high binding energies between the substrate and anion would facilitate the dissociation of sodium salt, thus releasing more free Na^+ ions for active charge transfer[10]. Moreover, the confined anion migration would increase the Na^+ ion transport number and enhance ionic conductivity, thereby leading to the enhanced migration kinetics. The computational results reveal that Bi_2S_3 and $NaBiS_2$ demonstrate higher binding energies of -1.78 eV and -1.83 eV than metallic substrates, suggesting a more pronounced affinity with PF_6 [Figure 5B]. On one hand, the strong interaction leads to the surface accumulation of anions and affects the solvation structure, thus avoiding the direct contact between solvent molecules and Na metal. On the other hand, the confined anion migration prolongs the duration of Na^+ nucleation stage, thereby allowing the refined grain nucleation and homogeneous Na deposition. Moreover, the strong binding with PF_6 anion would contribute to the construction of stable NaF-rich SEI, which thus suppresses the hazardous side reactions. Remarkably as revealed by the TOF-SIMS results, the significant content of NaF on the surface corroborate the calculation results. In addition, to investigate the stability of the artificial SEI layer, XPS analyses were performed on the Na-stripped Bi_2S_3@Cu electrode after 1 and 10 cycles [Supplementary Figure 6]. Note that the electrolyte of 1M $NaPF_6$ in DIGLYNE contains C, Na, O, F and P, which are the primary components of SEI layer, as confirmed by the XPS results. It's noteworthy that there is no significant variation of Na-F, Na-O, C-O and P-F bonds for the electrodes after 1 and 10 cycles, implying the high structure stability of the artificial SEI layer. However, in the S 2p XPS spectra, the S 2p peak is quite weak after 1 cycle and disappears after 10 cycles, suggesting Na_2S exists in the inner part, which is in agreement with the TOF-SIMS analysis.

To further demonstrate the efficacy of Na/Bi_2S_3 anode in practical application, full cells were constructed by paring with commercial NVP/C cathode (inset of Figure 6A). Figure 6A compares the cycling performances of the NVP/C‖Na/Bi_2S_3 and NVP/C‖Na full cells at 1 C (1 C = 117 mAh g^{-1}), and the NVP/C‖Na/Bi_2S_3 exhibits a higher specific capacity of 80 mAh g^{-1} with a higher retention of 84.5% after 300 cycles at 1 C, as compared with NVP/C‖Na cell using Na metal as anode (72 mAh g^{-1} with 80.0% retention). Figure 6B depicts the rate performances of both cells at different rates ranging from 2 C to 10 C, and NVP/C‖Na/Bi_2S_3 shows higher capacities under different rates than those for NVP/C‖Na, suggesting the better rate capability after intruding Bi_2S_3. Remarkably, NVP/C‖Na/Bi_2S_3 delivered a high specific capacity of 75.7 mAh g^{-1} even at 10 C (while 60.8 mAh g^{-1} for NVP/C‖Na), which can return to original value (88.3 mAh g^{-1}) after shifting back to 2 C (while 83.4 mAh g^{-1} for NVP/C‖Na). Moreover, Figure 6C and Supplementary Figure 7 show the corresponding charge-discharge profiles at various rates, and the full cells with Na/Bi_2S_3 anode showed well-defined plateau at around 3.4 V but with reduced polarization and low voltage hysteresis, suggesting the more stable and efficient electrochemical process of Na/Bi_2S_3 than that for the bare Na anode.

Figure 6D displays the long-term cycling stability of both full cells at a high rate of 10 C, the NVP/C‖Na/Bi_2S_3 full cell can survive for 2,500 cycles, delivering a capacity retention of 70% with a capacity decay rate of 0.012% per cycle. In contrast, the NVP/C‖Na full cell shows a rapid capacity fading with 37.2 mAh g^{-1} and 51% retention after 250 cycles under the same conditions. In addition, EIS was utilized to investigate the reaction kinetics of both kinds of full cells. As revealed by the Nyquist plots [Figure 6E], NVP/C‖Na/Bi_2S_3 displays a lower charge-transfer resistance (R_{ct}) of about 5 Ω than that of NVP/C‖Na (18 Ω, Supplementary Figure 8). Even after cycling at a high rate of 10 C, the R_{ct} remains at low values of 13 Ω after 100 cycles and 24 Ω after 1,000 cycles. Contrarily, the NVP/C‖Na cell showed a fast increased R_{ct} of 89 Ω after only 250 cycles. Such difference reveals that the bare Na anode undergoes great interfacial degradation upon cycling, probably because of thick SEI formation arising from the dendrite growth and inactive Na formation. These observations further reveal that the construction of Bi_2S_3 protective layer greatly contributed to the homogeneous and stable Na plating behavior, which finally enhanced the reaction kinetics and electrochemical performance of SMBs.

CONCLUSIONS

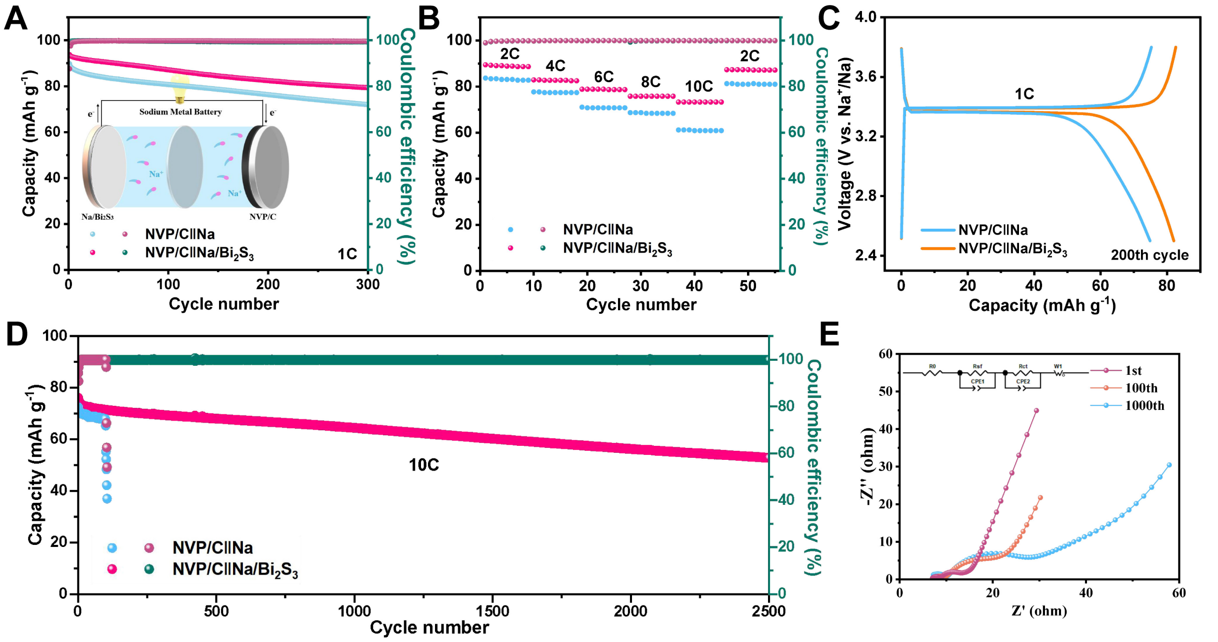

Figure 6. (A) Cycling performances at 1 C, (B) rate performances at different rates, (C) GCD profiles at 1 C, and (D) high-rate cycling performances at 10 C for the the NVP/C‖Na/Bi_2S_3 and NVP/C‖Na full cells; (E) Nyquist plots of the NVP/C‖Na/Bi_2S_3 full cells after different cycles with inset showing the corresponding equivalent circuit diagram. GCD: Galvanostatic discharge; NVP/C: $Na_3V_2(PO_4)_3$/C.

In summary, we have demonstrated the fabrication of Bi_2S_3 nanowires via a facile solvothermal route and their application as sodiophilic protective layers, which efficiently induced the uniform dendrite-free Na deposition. The Bi_2S_3 nanowires with higher Na adsorption energy underwent conversion-alloying reactions forming sodiophilic Na-Bi alloy sites and highly Na^+-diffusive Na_2S matrice, which synergistically lowered the Na nucleation barrier and enhanced Na^+ transfer kinetics, thus inhibiting the Na dendrite growth. Consequently, the Na/Bi_2S_3-based symmetric cell displayed exceptional long-term cycling stability upon repeated plating/stripping cycling (2,500 h with small voltage hysteresis of 15 mV at 2 mA cm^{-2} and 2 mAh cm^{-2}). Furthermore, the full cells consisting of commercial $Na_3V_2(PO_4)_3$/C cathode and Na/Bi_2S_3 anode demonstrated better cycling stability and higher rate performance than those for bare Na anode, implying the great potential in practical application. More importantly, this study validated Bi_2S_3 nanowires as an efficient sodiophilic modifier for SMAs, and proposed a scalable strategy for artificial SEI design- using metal chalcogenides as precursors to *in-situ* construct composite interfaces with alloy nucleation sites and ion-conductive matrices. This design provides valuable insights for developing dendrite-free alkali metal anodes and advancing the practical application of high-performance sodium metal batteries.

DECLARATIONS

Acknowledgments

The authors thank Ms Yan Liang at the Instrumental Analysis Center of Xian Jiaotong University for help with TOF-SIMS analysis.

Authors' contributions

Paper writing and experimental, data analysis: Li, J. (Jiazhe Li); Li, J. (Jiyi Li)
DFT calculation and review: Li, J. (Jiyi Li); Cao, D.
Normal analyses: Qiao, Y.; Ji, X.; Xue, W.; Xu, G.; Sun, H.; Han, X.
Core idea, data analysis, and supervision: Wang, H.

Availability of data and materials

The original data in this study are included in the article/Supplementary Materials. Further inquiries can be directed to the corresponding author(s).

AI and AI-assisted tools statement

During the preparation of this manuscript, the AI tool Grammarly Free (version Grammarly Inc., browser extension, accessed 2026-02) was used solely for language editing. The tool did not influence the study design, data collection, analysis, interpretation, or the scientific content of the work. All authors take full responsibility for the accuracy, integrity, and final content of the manuscript.

Financial support and sponsorship

The authors gratefully acknowledged the High-level Talent Research Start-up Project Funding of Henan Academy of Sciences (20251831004), Key Industrial Chain Technology Breakthrough Cluster Project of Xi'an City (25ZDLJQ00024), the Key Research and the Development Program of Shaanxi (2023QCY-LL-18), and the Innovation Capability Support Plan Project in Shaanxi Province (2024RS-CXTD-22).

Conflicts of interest

All authors declared that there are no conflicts of interest.

Ethical approval and consent to participate

Not applicable.

Consent for publication

Not applicable.

Copyright

Supplementary Materials

Supplementary Materials

REFERENCES

1. Turner, J. M. The matter of a clean energy future. *Science* **2022**, *376*, 1361-1361. DOI
2. Lukatskaya, M. R.; Dunn, B.; Gogotsi, Y. Multidimensional materials and device architectures for future hybrid energy storage. *Nat. Commun.* **2016**, *7*, 12647. DOI PubMed PMC
3. Yang, Z.; Zhang, J.; Kintner-Meyer, M. C.; et al. Electrochemical energy storage for green grid. *Chem. Rev.* **2011**, *111*, 3577-613. DOI
4. Xu, K. Electrolytes and interphases in Li-ion batteries and beyond. *Chem. Rev.* **2014**, *114*, 11503-618. DOI PubMed
5. Quilty, C. D.; Wu, D.; Li, W.; et al. Electron and ion transport in lithium and lithium-ion battery negative and positive composite electrodes. *Chem. Rev.* , *2023*, 1327-63. DOI
6. Wang, H.; Yang, X.; Wu, Q.; et al. Encapsulating silica/antimony into porous electrospun carbon nanofibers with robust structure stability for high-efficiency lithium storage. *ACS. Nano.* **2018**, *12*, 3406-16. DOI
7. Goodenough, J. B.; Kim, Y. Challenges for rechargeable Li batteries. *Chem. Mater.* **2010**, *22*, 587-603. DOI
8. Ruan, J.; Hu, J.; Li, Q.; et al. Current collector interphase design for high-energy and stable anode-less sodium batteries. *Nat. Sustain.* **2025**, *8*, 530-41. DOI
9. Chai, W.; Qiao, Y.; Wang, Z.; et al. HKUST-1 derived CuSx@C nanocomposites with TiO_2 coating and rich sulfur vacancies for excellent high-rate long-life sodium-ion batteries. *J. Power. Sources.* **2026**, *665*, 239009. DOI
10. Liu, P.; Miao, L.; Sun, Z.; Chen, X.; Jiao, L. Sodiophilic substrate induces NaF-rich solid electrolyte interface for dendrite-free sodium metal anode. *Adv. Mater.* **2024**, *36*, e2406058. DOI
11. Yu, Y.; Xu, S.; Yang, Y.; et al. Highly sodiophilic heterostructures toward dendrite-free sodium metal batteries. *Adv. Funct. Mater.* **2024**, *34*, 2401914. DOI
12. Rui, X.; Zhang, X.; Xu, S.; et al. A low-temperature sodium-ion full battery: superb kinetics and cycling stability. *Adv. Funct. Mater.* **2021**, *31*, 2009458. DOI
13. Huang, F.; Xu, P.; Fang, G.; Liang, S. In-depth understanding of interfacial Na^+ Behaviors in sodium metal anode: migration, desolvation, and deposition. *Adv. Mater.* **2024**, *36*, e2405310. DOI PubMed

14. Gao, W.; Lu, Y.; Tan, X.; et al. Sodiophilic design for sodium-metal batteries: progress and prospects. *Energy. Environ. Sci.* **2025**, *18*, 1630-57. DOI
15. Shi, D.; Lv, X.; Yang, Y.; et al. $NaBi_x/NaV_yO_z$ hybrid interfacial layer enables stable and dendrite-free sodium anodes. *Small* **2024**, *20*, e2402206. DOI
16. Damircheli, R.; Hoang, B.; Ferrari, V. C.; Lin, C. Highly uniform nitride-rich artificial solid electrolyte interphase enabled by nano-silicon nitride for superior performance in advanced sodium metal batteries. *J. Mater. Chem. A*. **2024**, *12*, 31949-58. DOI
17. Moorthy, M.; Thangavel, R.; An, S. Y.; Anilkumar, A.; Han, D.; Lee, Y. S. Recent trends in artificial SEI layers for controlling dendrite formation and enhancing cycle life: toward stable and durable sodium metal batteries. *Small* **2025**, *21*, e2502974. DOI PubMed PMC
18. Yin, H.; Cao, Y.; Wang, Y.; et al. Artificial solid electrolyte interphase for sodium metal batteries: mechanistic insights and design strategies. *Energy. Environ. Mater*. **2025**, *8*, e70077. DOI
19. Sun, H.; Zhu, G.; Xu, X.; et al. A safe and non-flammable sodium metal battery based on an ionic liquid electrolyte. *Nat. Commun.* **2019**, *10*, 3302. DOI PubMed PMC
20. Wu, Y.; Zhu, J.; Ni, J.; Li, L. Liquid metal-modified 3D Cu foam for dendrite-free sodium plating. *Small* **2024**, *20*, e2405357. DOI
21. Chen, R.; Lu, X.; He, Q.; et al. Sb_2S_3 nanorod hierarchies enabling homogeneous sodium deposition for dendrite-free sodium-metal batteries. *ACS. Appl. Energy. Mater*. **2022**, *5*, 10952-60. DOI
22. Hu, C.; Qi, J.; Zhang, Y.; et al. Room-temperature all-solid-state sodium battery based on bulk interfacial superionic conductor. *Nano. Lett.* **2021**, *21*, 10354-60. DOI
23. Chen, C.; Yao, W.; Tang, Y. Emerging solutions to enable the efficient use of sodium metal anodes: progress and perspectives. *Adv. Funct. Mater*. **2024**, *34*, 2310833. DOI
24. Chen, Q.; He, H.; Hou, Z.; et al. Building an artificial solid electrolyte interphase with high-uniformity and fast ion diffusion for ultralong-life sodium metal anodes. *J. Mater. Chem. A*. **2020**, *8*, 16232-7. DOI
25. Lu, X.; Chen, R.; Shen, S.; et al. Spatially confined in situ formed sodiophilic-conductive network for high-performance sodium metal batteries. *Nano. Lett.* **2024**, *24*, 5490-7. DOI
26. Xu, P.; Huang, F.; Liu, Z.; Guo, S.; Liang, S.; Fang, G. In situ construction of NaF-rich solid electrolyte interphase with metallic Ce sites for stable anode-free sodium metal batteries. *Angew. Chem. Int. Ed.* **2025**, *64*, e202515566. DOI
27. Li, Z.; Qin, H.; Tian, W.; et al. 3D Sb-based composite framework with gradient sodiophilicity for ultrastable sodium metal anodes. *Adv. Funct. Mater*. **2024**, *34*, 2301554. DOI
28. Li, Z.; Miao, L.; Lin, G.; et al. Na (100)-textured electrode embedded with Sb-doped SnO_2 nanoparticles for dendrite-free sodium metal batteries. *Adv. Energy. Mater*. **2024**, *14*, 2402284. DOI
29. Yang, G.; Li, N.; Sun, C. High-performance sodium metal batteries with sodium-bismuth alloy anode. *ACS. Appl. Energy. Mater*. **2020**, *3*, 12607-12. DOI
30. Su, D.; Dou, S.; Wang, G. Bismuth: a new anode for the Na-ion battery. *Nano. Energy*. **2015**, *12*, 88-95. DOI
31. Zhou, S.; Sun, Z.; Zhang, J.; et al. Single-atom engineering for synergistic nucleation and interfacial regulation enabling durable anode-free sodium metal batteries. *Adv. Mater*. **2026**, *38*, e13154. DOI
32. Kyono, A.; Kimata, M. Structural variations induced by difference of the inert pair effect in the stibnite-bismuthinite solid solution series $(Sb,Bi)_2S_3$. *Am. Mineral.* **2004**, *89*, 932-40. DOI
33. Li, Y.; Huang, L.; Li, B.; et al. Co-nucleus 1D/2D heterostructures with Bi_2S_3 nanowire and MoS_2 monolayer: one-step growth and defect-induced formation mechanism. *ACS. Nano.* **2016**, *10*, 8938-46. DOI
34. Yu, H.; Zhao, Y.; Zhang, J.; et al. Coordination regulation strategy in fabricating Bi_2S_3@CNFs composites with uniform dispersion for robust sodium storage. *Inorg. Chem.* **2024**, *63*, 21441-9. DOI
35. Yuan, M.; Wang, H.; Xu, T.; et al. Unlocking the ultrafast deposition kinetics within Bi-tailored core-shell structured carbon nanofibers for highly efficient and ultrastable sodium metal batteries. *Angew. Chem. Int. Ed.* **2025**, *64*, e202417930. DOI
36. Zhu, X.; Wang, Y.; Wang, W.; et al. Stable sodium metal anodes enabled by an in-situ generated mixed-ion/electron-conducting interface. *Chem. Eng. J.* **2022**, *446*, 136917. DOI
37. Ma, M.; Lu, Y.; Yan, Z.; Chen, J. In situ synthesis of a bismuth layer on a sodium metal anode for fast interfacial transport in sodium-oxygen batteries. *Batteries. Supercaps.* **2019**, *2*, 663-7. DOI
38. Moorthy, M.; Thangavel, R.; Ganesan, B. K.; et al. Ultra-high areal capacity, ultra-long life, dendrite-free sodium metal anode enabled by antimony-based Na-ion conducting artificial SEI layers. *Chem. Eng. J.* **2024**, *498*, 155234. DOI
39. Dai, J.; Wang, H.; Zhang, R.; et al. Co-sputtering strategy to construct robust sodiophilic interfaces for anode-less sodium metal batteries. *Chem. Commun.* **2024**, *60*, 11120-3. DOI
40. Arab, J.; Mishra, D. K.; Kannojia, H. K.; Adhale, P.; Dixit, P. Fabrication of multiple through-holes in non-conductive materials by electrochemical discharge machining for RF MEMS packaging. *J. Mater. Process. Technol.* **2019**, *271*, 542-53. DOI

41. Sun, B.; Li, P.; Zhang, J.; et al. Dendrite-free sodium-metal anodes for high-energy sodium-metal batteries. *Adv. Mater.* **2018**, *30*, 1801334. DOI
42. He, G.; Xiao, Y.; Zhang, T.; et al. Localized solvent-anchored carboxylate ester electrolyte enables wide temperature and fast charging sodium metal batteries. *Adv. Mater.* **2026**, *38*, e23324. DOI
43. Zhang, W.; Lu, Q.; Sun, G.; et al. Sodiophilic interface induces a NaF-rich solid electrolyte interface for stable sodium-metal batteries under harsh conditions. *Nano. Lett.* **2025**, *25*, 6092-100. DOI
